Supplementary information for

Harnessing dual forms of water energy for all-weather high-performance electricity generation using amorphous slurry

Wenna Ge[†a], Quanmao Wei[†a], Wenzong Li[a], Xu Wang[a], Chenguang Lu[a], Keke Zhang[a], Xuanqi Luo[a], Lemin Zhang[ab], Yu Sun*[cd], Yahua Liu*[ab]

[a]*State Key Laboratory of High-performance Precision Manufacturing, Dalian University of Technology, Dalian, 116024, P. R. China.*

[b]*Department of Anaesthesiology, Central Hospital of Dalian University of Technology, Dalian, 116033, PR China.*

[c]*Department of Mechanical and Industrial Engineering, University of Toronto, Toronto, Ontario M5S 3G8, Canada.*

[d]*Department of Electrical and Computer Engineering, University of Toronto, Toronto, Ontario M5S 3G4, Canada.*

[†]*These authors contributed equally to this work.*

E-mail: yahualiu@dlut.edu.cn (Y.L.); yu.sun@utoronto.ca (Y.S.)

Note S1. Density functional theory simulation

The hydration free energy of the proton was theoretically determined by density functional theory simulation (DFT) using a commercial Gaussian 16 software package. Specifically, the solvation model density (SMD) solvation model was adopted to describe the solvation environments, and geometry optimizations were carried out using the B3LYP/6-311G* basis set. Single-point energy calculations were performed using M052X/6-31G* basis set to obtain accurate electronic energies for its specific accuracy in the calculations of solvation free energy[1]. Based on previous studies[2], the hydration process of proton can be described as the following equation:

$$H^+(gas) + (H_2O)_n(aq) \rightarrow H_3O^+(H_2O)_{n-1}(aq) \quad (1)$$

Where $H^+(gas)$, $(H_2O)_n(aq)$, and $H_3O^+(H_2O)_{n-1}(aq)$ are the proton, the solution, and hydrated solution, respectively. To calculate the free energy for reaction (1), the Gibbs free energy of $H^+(gas)$, $(H_2O)_n(aq)$, and $H_3O^+(H_2O)_{n-1}(aq)$ must first be obtained. The free energy of $H^+(gas)$, i.e. $G[H^+(gas)]$, has been calculated by well-established methods[2,3] to be – 6.3 kcal/mol. The free energies of $H_3O^+(H_2O)_{n-1}(aq)$ and $(H_2O)_n(aq)$, i.e., $G[H_3O^+(H_2O)_{n-1}(aq)]$ and $G[(H_2O)_n(aq)]$, can be calculated using the SMD solvation model at the M052X/6-31G* level. Then the hydration free energy of the proton ($\Delta G_{hyd}(H^+, n)$) can be calculated as

$$\Delta G_{hyd}(H^+, n) = G[H_3O^+(H_2O)_{n-1}(aq)] - G[(H_2O)_n(aq)] - G[H^+(gas)] \quad (2)$$

Where $G[H_3O^+(H_2O)_{n-1}(aq)]$, $G[(H_2O)_n(aq)]$, and $G[H^+(gas)]$ represent the free energies of hydrated solution (with implicit solvent model), the solution (with implicit solvent model) and the proton (without implicit solvent model), respectively.

Supplementary Figures

The natural seaweed mud, consisting of microbes, organic and inorganic matters agglomerated in a network by extracellular polymeric substances, spontaneously absorbed water from ambient moisture, increasing its mass by 165.9 wt% at 90% RH (Figure S1a). When assembled with a porous Ag electrode and a carbon tap electrode, it generated a V_{oc} of ~ 0.5 V (Figure S1b). Moreover, it delivered a V_{oc} of 0.13 V by evaporating retention water at 5% RH. Different from traditional hygroscopic films, the amorphous structure allowed the seaweed mud to maintain its morphology after adding droplets, providing a foundation for harvesting energy from liquid water (Figure S2). Thus, the natural seaweed mud effectively harvested energy from both liquid water and moisture, serving as an ideal prototype for designing the DWEG.

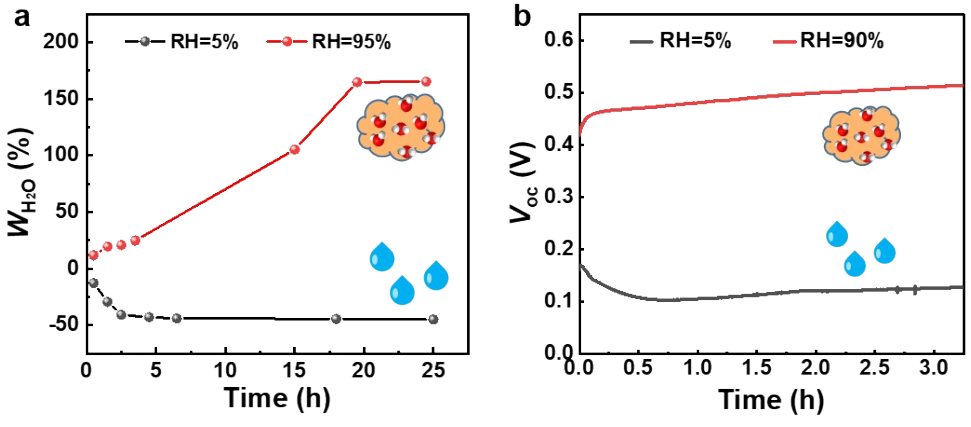

Figure S1. The energy-harvesting properties of natural seaweed mud. a) Moisture absorption and water evaporation kinetics for the seaweed mud at 90% RH and after adding a droplet at 5% RH, respectively. b) V_{oc} curves of the generator constructed by the seaweed mud at the same condition.

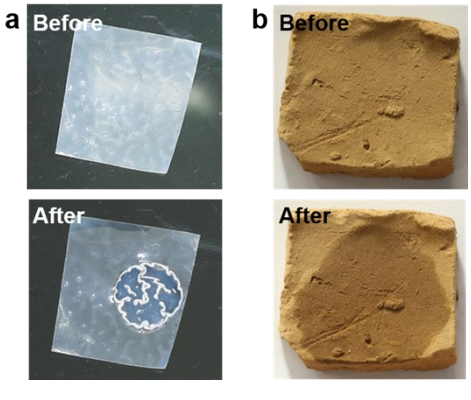

Figure S2. The morphology of traditional CNC/PVA film (a) and natural seaweed mud (b), before and after adding pure water.

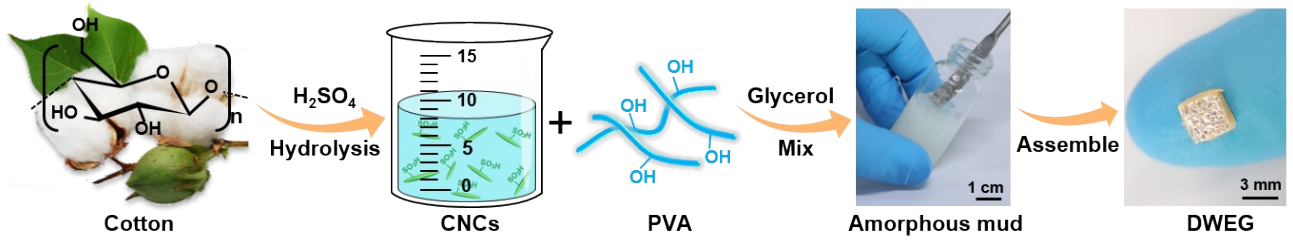

Figure S3. Schematics showing the preparation process of the amorphous slurry.

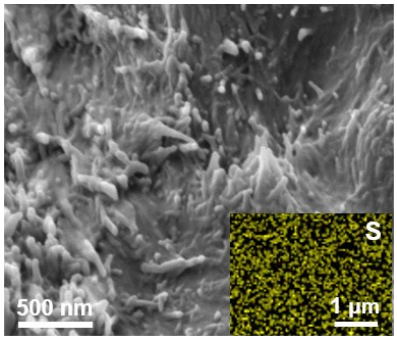

Figure S4. Scanning electron microscopic image of the amorphous slurry. The inset is the element mapping images of the sulfur.

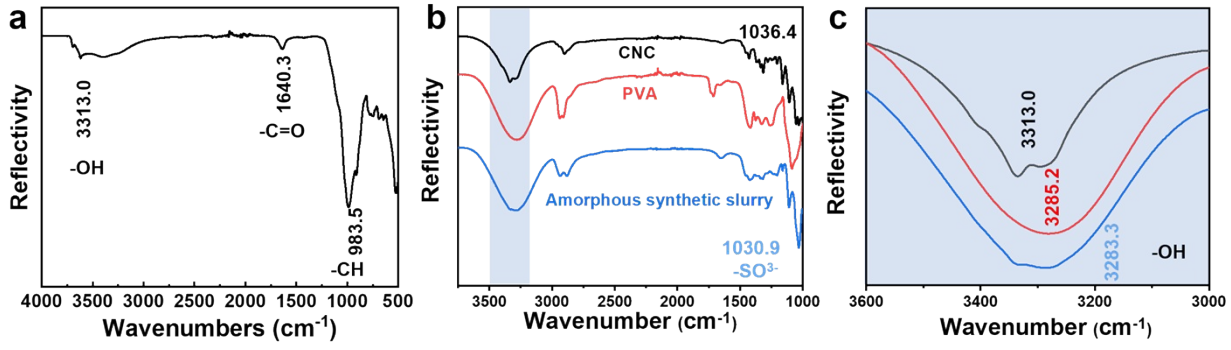

Figure S5. FTIR spectroscopy analysis. (a) FTIR spectra of the seaweed mud. (b) FTIR spectra of CNC, PVA, and amorphous slurry. (c) An enlarged view of the hydroxyl absorption peak. The seaweed mud showed peaks at 3621.8 cm^{-1}, 1640.3 cm^{-1}, and 983.5 cm^{-1}, indicating the presence of hydroxyl, carboxyl, and methyl groups. The amorphous slurry exhibited peaks at 3283.3 cm^{-1} and 1030.9 cm^{-1}, corresponding to hydroxyl and sulfonic acid groups. Sulfonic acid groups are ionic functional groups that can dissociate mobile H^+ upon interaction with water molecules.

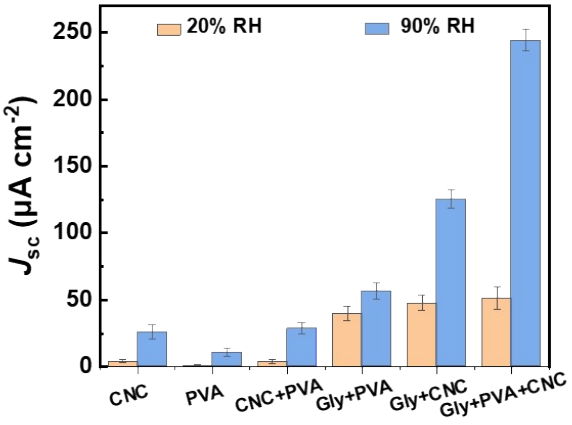

Figure S6. The current density of the generators with different hybrid systems at 20% RH and 90% RH.

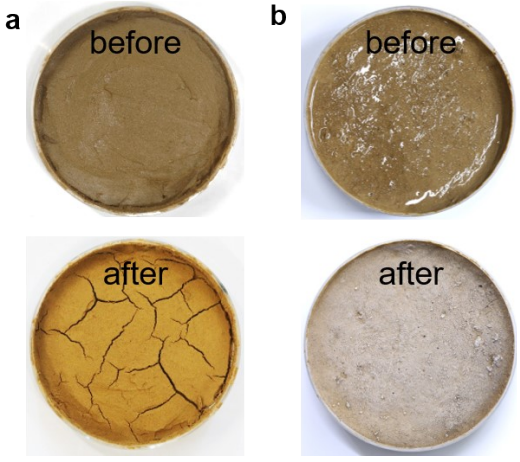

Figure S7. The morphology of the seaweed mud. Cracks (a) and ice-crystals (b) appeared on the surface of the seaweed mud after 10 hours of water evaporation at 5% RH and exposure at –7 °C, respectively.

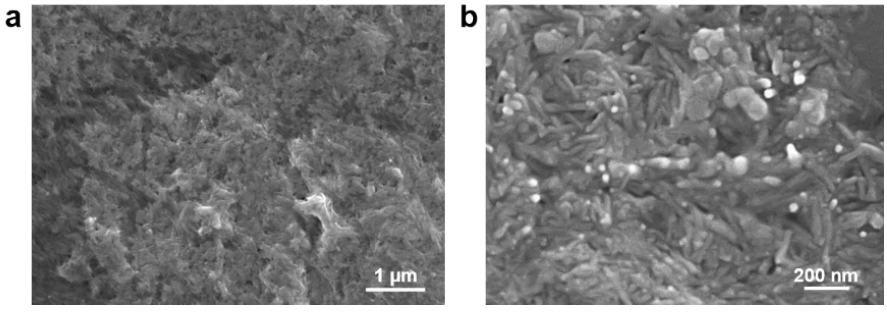

Figure S8. Morphological characterization of the desolvated slurry. (a) SEM image showing the porous network structure. (b) Higher-magnification view revealing the stacked arrangement of fusiform cellulose nanocrystals.

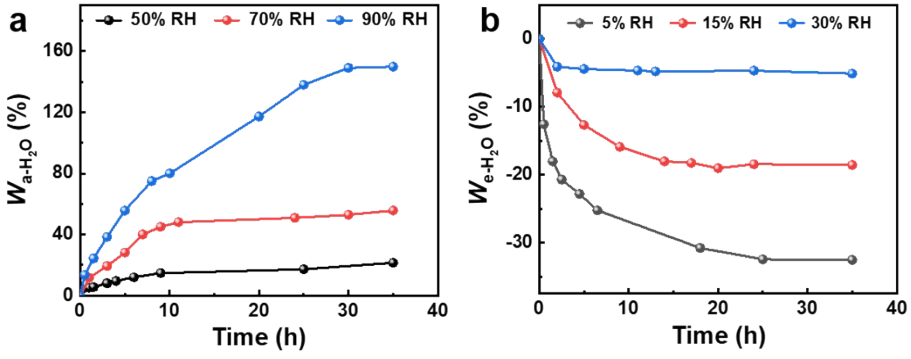

Figure S9. Water molecules exchange kinetics for the DWEG at different RH. (a) Mass change of the DWEG at 50%, 70%, and 90% RH. (b) Mass change of the DWEG at 5%, 15% and 30% RH.

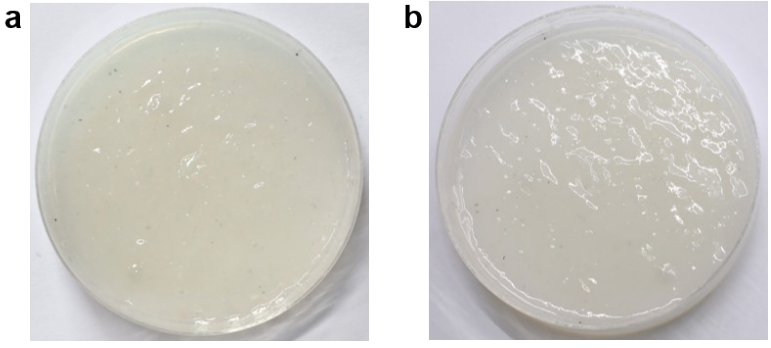

Figure S10. The morphology of the amorphous slurry. Morphology of the amorphous slurry before (a) and after (b) adding liquid water. The amorphous slurry maintained its stable structure after the droplet was added, providing a crucial foundation for the DWEG to harvest energy from liquid water.

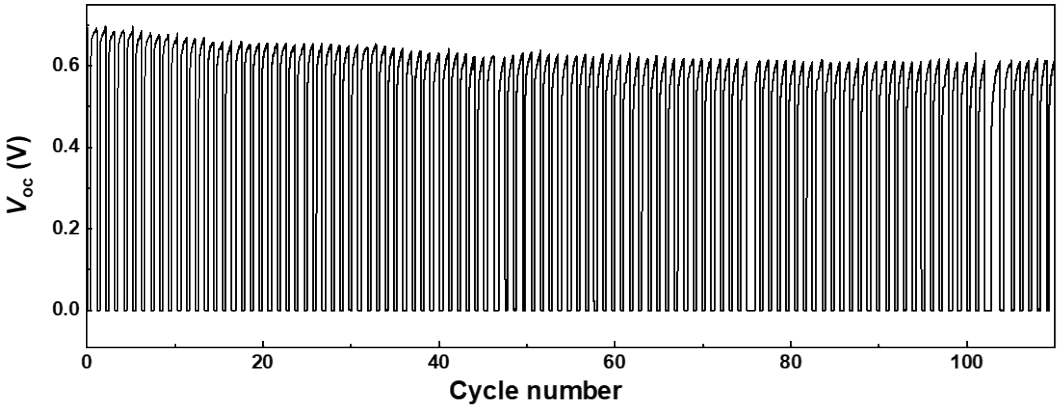

Figure. S11. The charge–discharge cycle curves of the DWEG.

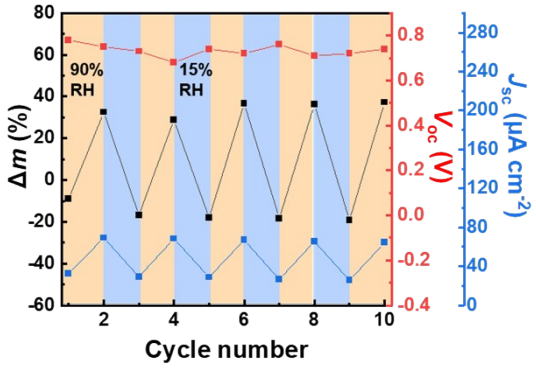

Figure. S12. The adsorption–dehydration cycle curves of the DWEG.

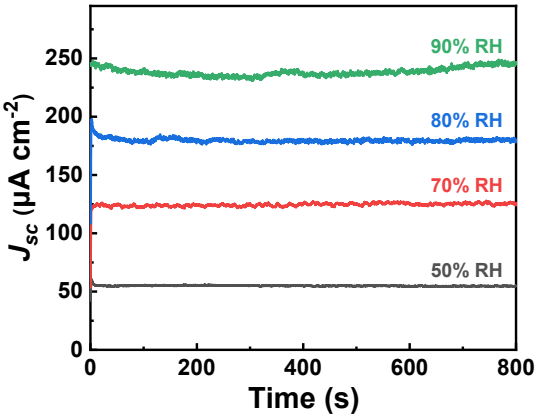

Figure S13. The curves of I_{sc} versus time under different RH at 25 °C.

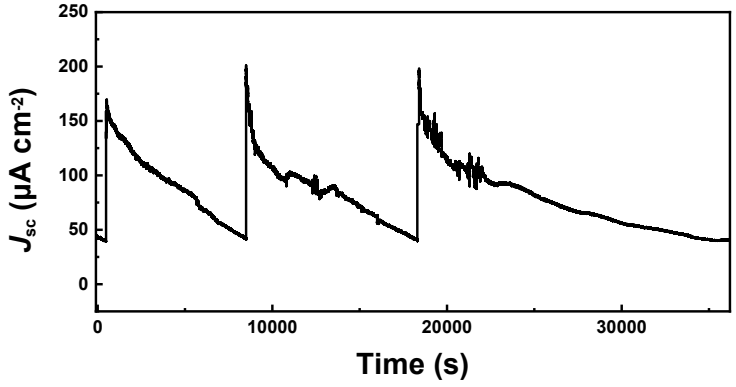

Figure S14. J_{sc} response to periodic 15-μL water droplet additions.

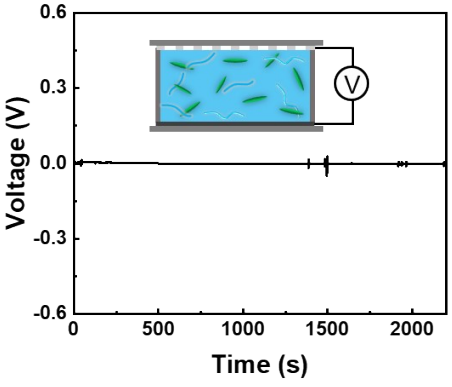

Figure S15. Near-zero voltage was produced by the DWEG with both top and bottom surfaces sealed.

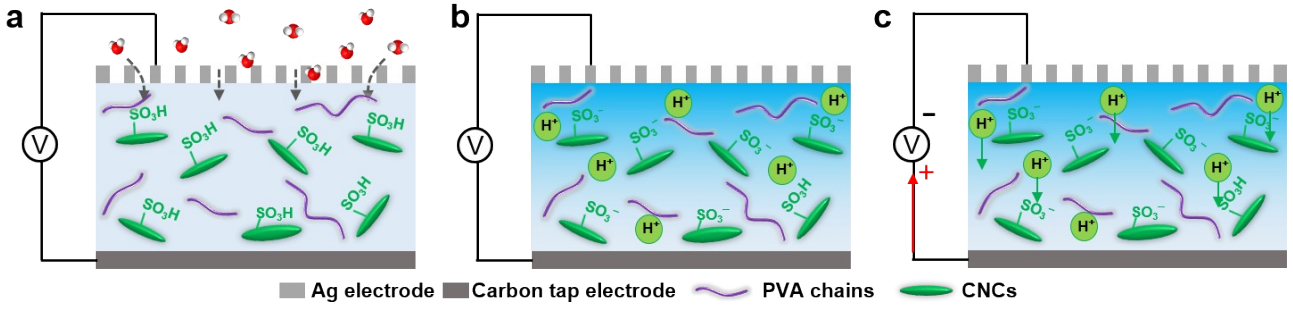

Figure S16. Schematic showing the electricity generation process of the DWEG based on a water gradient. The electricity generation during moisture absorption involves three stages including moisture adsorption (a), ion dissociation (b), and ion diffusion (c). As moisture passes through the porous top Ag electrode but is blocked by the bottom carbon tap electrode, a water gradient is spontaneously established within the amorphous slurry. Meanwhile, H^+ ions dissociated from the sulfonic acid groups, creating an ion concentration gradient. The mobile H^+ ions, driven by this gradient, diffuse from top to bottom, generating electric potential and current flow.

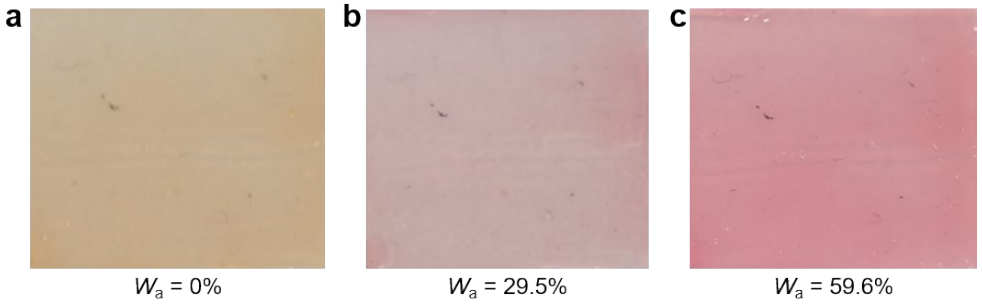

Figure S17. The color of the amorphous slurry with different moisture absorption ratio W_a. As the moisture absorption ratio increased from 0% to 59.6%, the amorphous slurry, mixed with an acid indicator, undergoes a sequential color transition from yellow (a) to pink (b) and finally to red (c).

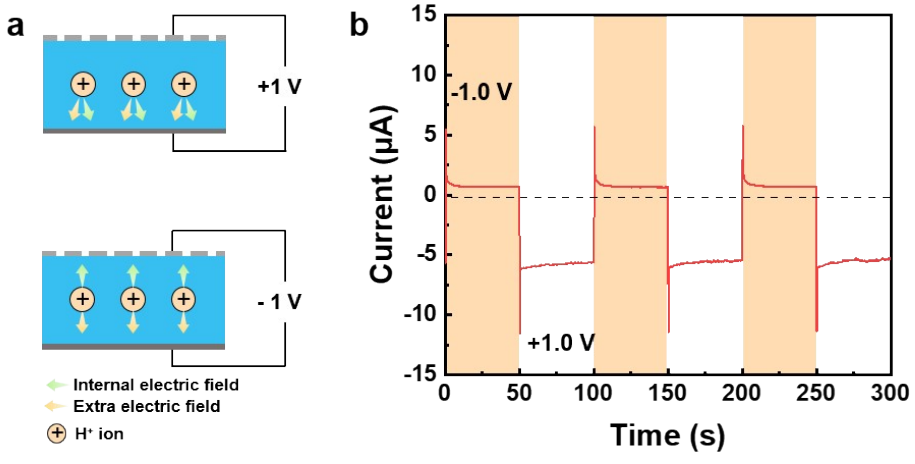

Figure S18. The ion rectification of the DWEG under an alternating bias voltage of ±1.0 V at 15% RH. (a) Schematic showing the ion diffusion within the DWEG under an alternating bias voltage of ±1.0 V. (b) The current response curves of the DWEG under an alternating bias voltage of ±1.0 V at 15% RH.

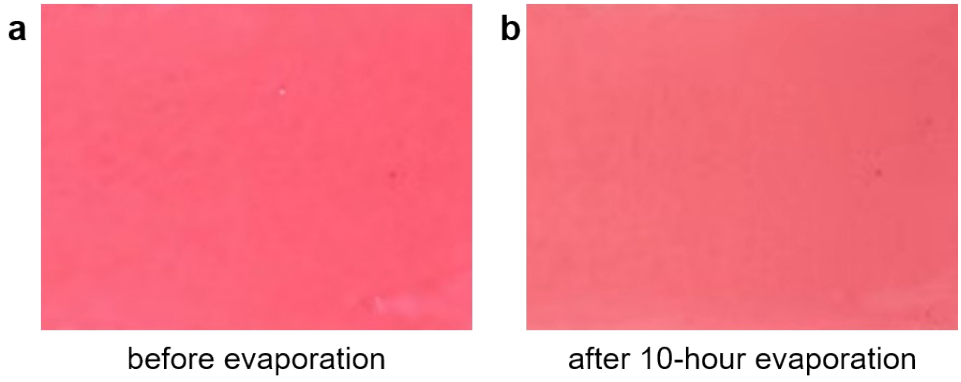

Figure S19. The color of the amorphous slurry mixed with the acid indicator before (a) and after (b) 10-hour evaporation at 25% RH. The amorphous slurry remains red after 10-hour evaporation at 25% RH.

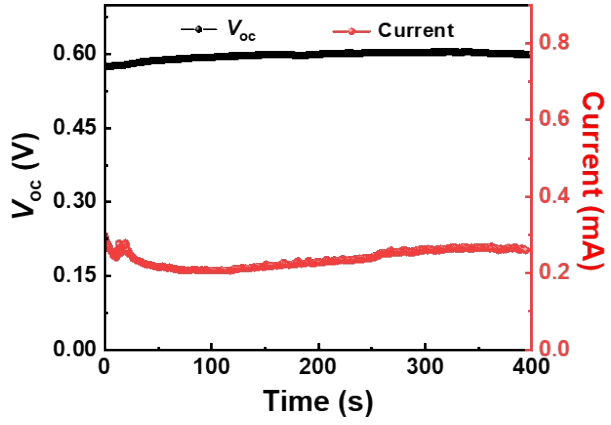

Figure S20. The curves of V_{oc} and current generated by a DWEG array with 2.0 cm × 7.0 cm.

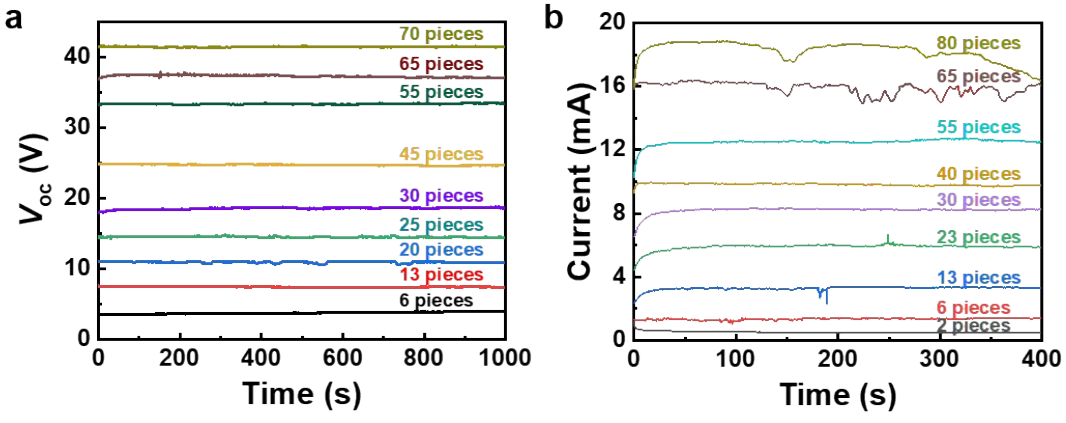

Figure S21. The output performance of integrated DWEG arrays with 2.0 cm × 7.0 cm in serial or parallel at 50% ± 5% RH and 25 °C. a) V_{oc} of a serial DWEG arrays with different series number. b) Current output of a parallel DWEG arrays with different parallel number.

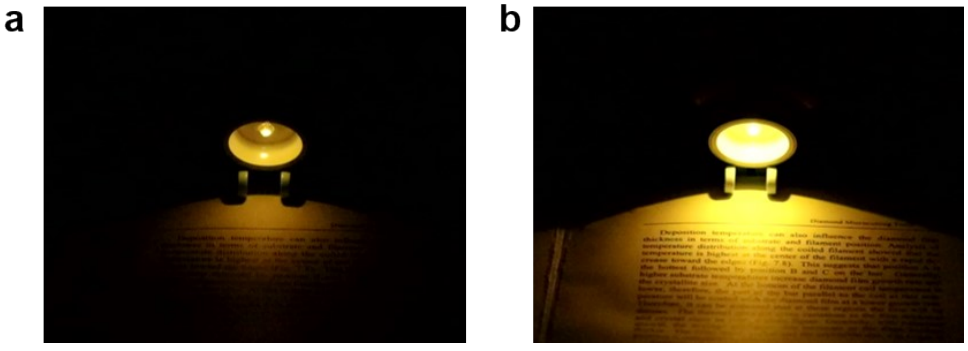

Figure S22. Photographs of the table lamp brightness. Photographs of the table lamp brightness after working for six days (a) and repaired by adding water droplets (b).

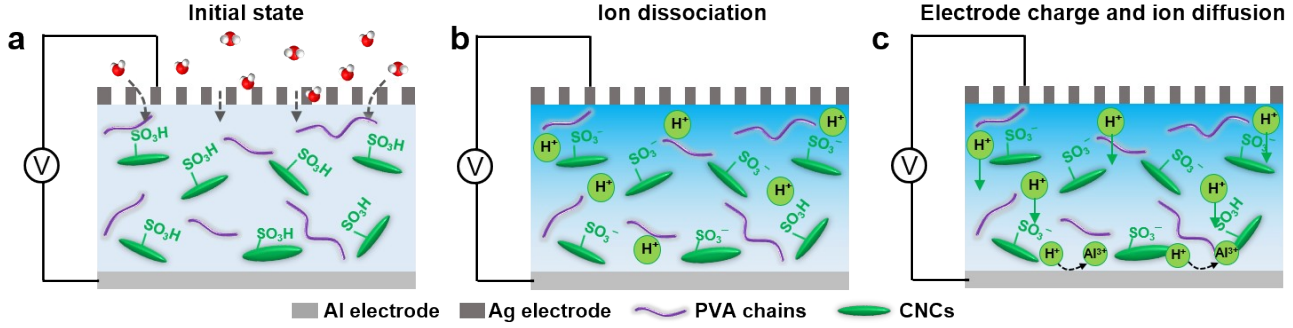

Figure S23. Schematic showing the working mechanism of the DWEG with Al and Ag electrodes. a) The amorphous slurry spontaneously absorbs water molecules from the surrounding moisture. b) The absorbed water molecules interact with the -SO_3H functional group, leading to H^+ ions dissociation and creating an ion concentration gradient. c, As H^+ ions near the Al electrode reacts with it, some H^+ ions are consumed, further amplifying the ion concentration gradient and accelerating ion diffusion.

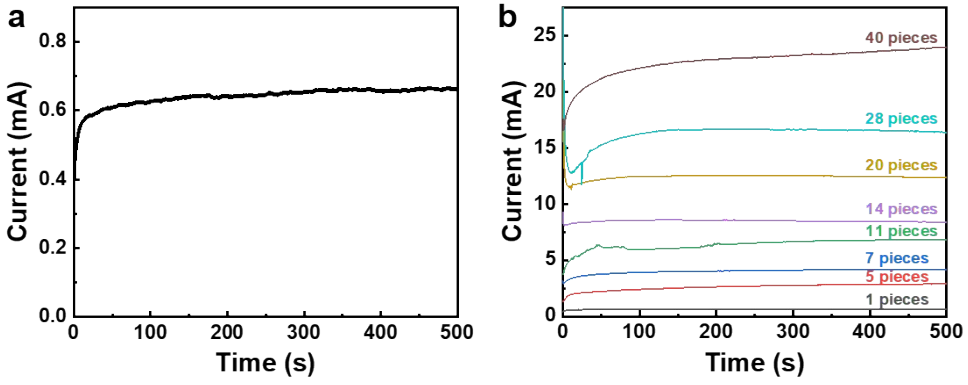

Figure S24. The current output of parallel DWEG arrays with assembled Al and Ag electrodes. a) The current of a single DWEG unit under laboratory conditions. b) The current of parallel DWEG arrays under the same condition.

Table S1. Output performance of hydrovoltaic generators at a RH above 90%

No.	Hygroscopic material	Humidity conditions	V_{oc} (V)	J_{sc} (μA cm^{-2})	Holding time (h)	Reference
1	PAAS* + DMA-PAA-Q*	90%	0.05	0.029	44.4	[4]
2	Carbon	95%	0.068	0.0006	6	[5]
3	CNF*	99%	0.11	0.022	167	[6]
4	CNF*	99%	0.115	0.004	0.67	[7]
5	SilkNFs*	99%	0.12	0.008	0.67	[8]
6	PAN* + SDBS* + DTAB*	95%	0.7	1.33	120	[9]
7	GO* + FGO*	99%	1.25	—	12.5	[10]
8	Protein nanofibrils	90%	0.65	1.93	8	[11]
9	SA* + SiO_2 + rGO*	100%	0.5	112.3	3.3	[12]
10	PSS* + H_2SO_4	90%	0.8	120	12	[13]
11	CNCs + PVA + Gly	90%	0.73	258	420	**This work**

*GO: graphene oxide; *FOG: fluorinated oxidized graphene; *SDBS: Sodium dodecyl benzene sulfonate; *DTAB: dodecyl trimethylammonium bromide; *PSS: polystyrene sulfonic acid; CNF: cellulose nanofibrous; PAAS: poly (sodium 4-styrene sulfonate); *DMA-PAA-Q: 3-acrylamidopropyl[trimethylammonium] chloride; *PAN: polyacrylonitrile; *SA: sodium alginate; *rGO: reduced graphene oxide; *SlikNFs: silk nanofibrils

Table S2. Output power density of hydrovoltaic generators

No.	Hygroscopic material	Humidity conditions	Area (cm^2)	V_{oc} (V)	J_{sc} ($\mu A/cm^2$)	Output power (μW)	Power density ($\mu W\ cm^{-2}$)	Reference
1	GO*	85%	0.04	0.45	4.5	0.008	0.2	14
2	GO*	80%	0.1	0.6	1.2	0.7	7	15
3	Protein nanowires	50%	0.25	0.5	1.6	1.25	5	16
4	whole-cell	75%	0.04	0.3	7.5	0.1	2.5	17
5	PSSA* + PDDA*	25%	0.04	0.95	0.2	0.005	1.25	18
6	PAN + SDBS* + DTAB*	95%	2.25	0.7	1.3	0.15	0.067	9
7	Cellulose	60%	9	0.78	0.83	1.47	0.16	19
8	PA* + PVA + Gly	85%	0.25	0.8	240	8.75	35	20
9	Protein nanofibers	90%	0.02	0.65	150	0.776	38.8	11
10	PSS* + PVA	80%	1	1	1.7	0.1	0.1	21
11	Nb_2CT_x/SA*	91.5%	0.25	0.55	1.6	0.125	0.5	22
12	PSSA* + PDDA*	80%	0.3	1.1	11.3	0.78	2.6	23
13	Sludge	90%	1.5	0.45	1.98	0.21	0.14	24
14	CNF*	99%	1	0.12	0.022	0.62	0.62	6
15	PSS* + H_2SO_4	90%	0.16	0.8	120	3.25	20.3	13
16	PAM* + AMPS* + LiCl	80%	0.25	0.8	480	13.32	53.28	25
17	CNC + PVA + Gly	90%	0.09	0.7	258	2.88	32	**This work**

Table S3. Output performance of hydrovoltaic generators at a RH below 35%

No.	Hygroscopic material	Humidity conditions	Area (cm^2)	V_{oc} (V)	J_{sc} ($\mu A\ cm^{-2}$)	Output type	Reference
1	GO*	25%	0.25	0.32	0.09	Continuous	14
2	TiO_2 nanowire	20%	1.44	0.02	0.05	Transient	26
3	PSSA* + PDDA*	25%	0.6	0.95	0.08	Continuous	18
4	PAN* + SDBS* + DTAB*	35%	2.25	0	0	Continuous	9
5	PA* + PVA + Gly	10%	0.25	0.2	0.32	Continuous	20
6	CA*	27%	4	0.03	0.07	Continuous	27
7	Textile + PSS* + PVA	20%	1	0.3	0.32	Continuous	21
8	SA + SiO_2 + rGO*	15%	0.89	0.5	56	Transient	12
9	CNW*/LiCl + PAN* + P(VDF-TrFE)*	15%	2	0.7	2.5	Continuous	28
10	PSSA* + PVA + LiCl + Gly	10%	4	0.65	0.13	Continuous	29
11	PVA + LiCl + PA*	20%	1	0.42	5	Continuous	30
12	CNCs + PVA + Gly	5%	0.09	0.76	228	Continuous	**This work**

*CA: Citric acid; *PA: Phytic acid; *CNW: Cellulose nonwoven; *P(VDF-TrFE): poly(vinylidene fluoride-trifluoroethylene);

Reference

1. J. Ho, A. Klamt and M. L. Coote, *J. Phys. Chem. A*, 2010, **114**, 13442-13444.
2. C. Z. D. A. Dixon, *J. Phys. Chem. A*, 2001, **105**, 11534-11540.
3. G. J. Tawa, I. A. Topol, S. K. Burt, R. A. Caldwell and A. A. Rashin, *J. Chem. Phys.*, 1998, **109**, 4852-4863.
4. W. Lu, T. Ding, X. Wang, C. Zhang, T. Li, K. Zeng and G. W. Ho, *Nano Energy*, 2022, **104**, 107892.
5. K. Liu, P. Yang, S. Li, J. Li, T. Ding, G. Xue, Q. Chen, G. Feng and J. Zhou, *Angew. Chem.-Int. Edit.*, 2016, **55**, 8003-8007.
6. M. Li, L. Zong, W. Yang, X. Li, J. You, X. Wu, Z. Li and C. Li, *Adv. Funct. Mater.*, 2019, **29**, 1901798.
7. W. Yang, X. Li, X. Han, W. Zhang, Z. Wang, X. Ma, M. Li and C. Li, *Nano Energy*, 2020, **71**, 104610.
8. W. Yang, L. Lv, X. Li, X. Han, M. Li and C. Li, *ACS Nano*, 2020, **14**, 10600-10607.
9. Z. Sun, X. Wen, L. Wang, J. Yu and X. Qin, *Energy Environ. Sci.*, 2022, **15**, 4584-4591.
10. K. Fan, X. Liu, Y. Liu, Y. Li, X. Liu, W. Feng and X. Wang, *Nano Energy*, 2022, **91**, 106605.
11. J. Liu, L. Huang, W. He, X. Cai, Y. Wang, L. Zhou and Y. Yuan, *Nano Energy*, 2022, **102**, 107709.
12. H. Wang, T. He, X. Hao, Y. Huang, H. Yao, F. Liu, H. Cheng and L. Qu, *Nat. Commun.*, 2022, **13**, 2524.
13. Y. Huang, K. Zhou, H. Cheng, T. He, H. Wang, J. Bai, C. Yang, T. Guang, H. Yao, F. Li, G. Hou, Z. Xu and L. Qu, *Adv. Funct. Mater.*, 2023, **34**, 2308620.
14. H. Cheng, Y. Huang, F. Zhao, C. Yang, P. Zhang, L. Jiang, G. Shi and L. Qu, *Energy Environ. Sci.*, 2018, **11**, 2839-2845.
15. Y. Huang, H. Cheng, C. Yang, H. Yao, C. Li and L. Qu, *Energy Environ. Sci.*, 2019, **12**, 1848-1856.
16. X. Liu, H. Gao, J. E. Ward, X. Liu, B. Yin, T. Fu, J. Chen, D. R. Lovley and J. Yao, *Nature*, 2020, **578**, 550-554.
17. G. Ren, Z. Wang, B. Zhang, X. Liu, J. Ye, Q. Hu and S. Zhou, *Nano Energy*, 2021, **89**, 106361.
18. H. Wang, Y. Sun, T. He, Y. Huang, H. Cheng, C. Li, D. Xie, P. Yang, Y. Zhang and L. Qu, *Nat. Nanotechnol.*, 2021, **16**, 811-819.
19. J. Tan, S. Fang, Z. Zhang, J. Yin, L. Li, X. Wang and W. Guo, *Nat. Commun.*, 2022, **13**, 3643.
20. S. Yang, X. M. Tao, W. Chen, J. F. Mao, H. Luo, S. P. Lin, L. S. Zhang and J. H. Hao, *Adv. Mater.*, 2022, **34**, 2200693.
21. W. He, H. Wang, Y. Huang, T. He, F. Chi, H. Cheng, D. Liu, L. Dai and L. Qu, *Nano Energy*, 2022, **95**, 107017.
22. Q. Zhao, Y. Jiang, Z. Duan, Z. Yuan, J. Zha, Z. Wu, Q. Huang, Z. Zhou, H. Li and F. He, *Chem. Eng. J.*, 2022, **438**, 135588.
23. T. He, H. Wang, B. Lu, T. Guang, C. Yang, Y. Huang, H. Cheng and L. Qu, *Joule*, 2023, **7**, 935-951.
24. J. Liu, X. Cai, Y. Wang, G. Ren, L. Zhou, M. Mahmoud, S. Zhou and Y. Yuan, *Chem. Eng. J.*, 2023, **472**, 144868.
25. H. Zhang, N. He, B. Wang, B. Ding, B. Jiang, D. Tang and L. Li, *Adv. Mater.*, 2023, **35**, 2300398.
26. D. Shen, M. Xiao, G. Zou, L. Liu, W. W. Duley and Y. N. Zhou, *Adv. Mater.*, 2018, **30**, 1705925.
27. L. Yang, L. Zhang and D. Sun, *ACS Appl. Mater. Interfaces*, 2022, **14**, 53615-53626.
28. Y. H. Hu, W. F. Yang, W. Wei, Z. Q. Sun, B. Wu, K. R. Li, Y. G. Li, Q. H. Zhang, C. Y. Hou, and H. Z. Wang, *Sci. Adv.*, 2024, **10**, eadk4620.

29. J. Lu, B. Xu, J. Huang, X. Liu and H. Fu, *Adv. Funct. Mater.*, 2024, **34**, 2406901.
30. C. Guo, H. Tang, P. Wang, Q. Xu, H. Pan, X. Zhao, F. Fan, T. Li and D. Zhao, *Nat. Commun.*, 2024, **15**, 6100.